

Supplementary Information

Giant anomalous Hall effect in a ferromagnetic Kagomé-lattice semimetal

Enke Liu^{1,2*}, Yan Sun^{1*}, Nitesh Kumar¹, Lukas Muechler³, Aili Sun¹, Lin Jiao¹, Shuo-Ying Yang⁴, Defa Liu⁴, Aiji Liang^{5,6}, Qiunan Xu¹, Johannes Kroder¹, Vicky Süß¹, Horst Borrmann¹, Chandra Shekhar¹, Zhaosheng Wang⁷, Chuanying Xi⁷, Wenhong Wang², Walter Schnelle¹, Steffen Wirth¹, Yulin Chen^{5,8}, Sebastian T. B. Goennenwein⁹ and Claudia Felser^{1*}

¹ Max Planck Institute for Chemical Physics of Solids, Dresden, Germany

² Institute of Physics, Chinese Academy of Sciences, Beijing, China

³ Department of Chemistry, Princeton University, Princeton, New Jersey, USA

⁴ Max Planck Institute of Microstructure Physics, Halle, Germany

⁵ School of Physical Science and Technology, ShanghaiTech University, Shanghai, China

⁶ Advanced Light Source, Lawrence Berkeley National Laboratory, Berkeley, California, USA

⁷ High Magnetic Field Laboratory, Chinese Academy of Sciences, Hefei, Anhui, China

⁸ Clarendon Laboratory, Department of Physics, University of Oxford, Parks Road, Oxford, UK

⁹ Institut für Festkörper- und Material Physik, Technische Universität Dresden, Dresden, Germany

* e-mail: ekliu@iphy.ac.cn; Yan.Sun@cpfs.mpg.de; Claudia.Felser@cpfs.mpg.de

1. Single-crystal growths

The single crystals of $\text{Co}_3\text{Sn}_2\text{S}_2$ can be grown by several methods¹⁻³. In 2012, P. C. Canfield's group has grown this S-based crystal by self-flux method and reported some basic data on this compound¹. In present study, we grew the crystals by two different self-flux methods. One is the method with the congruent composition. The other one is the method with Sn as flux^{1,3}. For the congruent composition, the samples were included in a graphite crucible sealed in a quartz tube. The stoichiometric samples (Co : Sn : S = 3 : 2 : 2) were heated to 1000 °C over 48 hours and kept there for 24 hours before being slowly cooled to 600 °C over 7 days. Some iodine was added to the samples for better reactions between the elements for homogenous alloying. The compositions of crystals were checked by energy dispersive X-ray spectroscopy (EDS). The composition of crystals is Co : Sn : S = 2.93 : 2 : 2, which is slightly lower than the nominal composition and is expected to show a slight p-doped effect on the transport behaviour.



Fig. S1. Optical image of big single crystals grown by self-flux method with congruent composition. The flat cleaved surface on the left hand is the a - b plane of the crystal.

2. Structural characterizations

2.1 X-ray diffraction

The crystals were characterized by powder X-ray diffraction as single phase with a Shandite-type structure. Derived lattice parameters at room temperature are $a = 5.3689 \text{ \AA}$ and $c = 13.176 \text{ \AA}$ in hexagonal setting. Single crystals and orientations were assigned by single-crystal X-ray diffraction technique. However, we found that an unambiguous assignment of the threefold axis is virtually impossible without careful analysis of Bragg intensities. This is due to a very particular situation as the unit cell is virtually cubic but also the arrangement of atoms in the structure show very little or no deviation, respectively, from cubic symmetry. Accordingly deviations in intensities of Bragg peaks are reflected in a small subset and quite hard to identify (Fig. S2b). As a final confirmation of the assignments a full data set was collected and the established model was refined (Table S1).

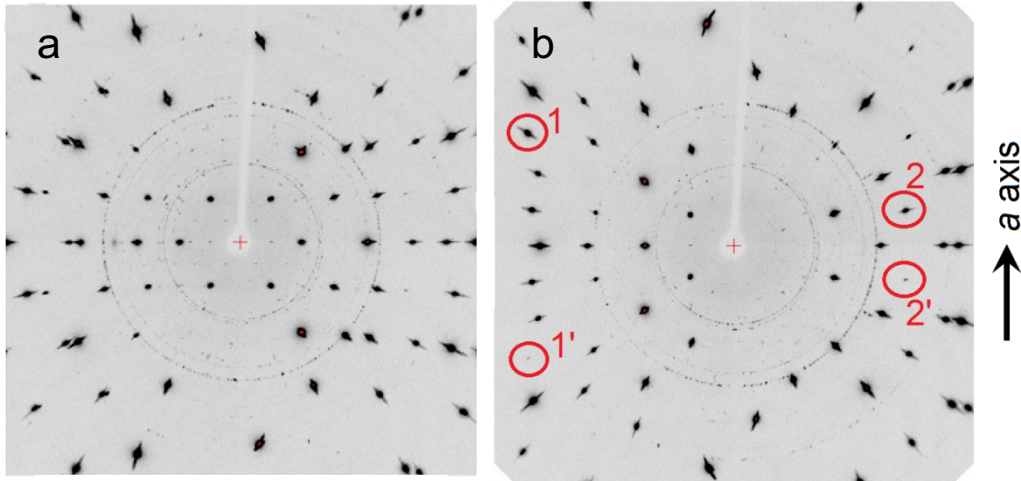


Fig. S2. Single-crystal XRD pattern observed at room temperature. (a) Single-crystal XRD pattern after rocking by 32° about a -axis of the rhombohedral cell. Sharp and distinct diffraction spots prove the high quality of the crystal. The faint powder rings may be assigned to distortions and contaminations on the surface. (b) Oscillation image taken while rocking the crystal by 32° about the a -axis of the FCC type cell. Spots violating horizontal mirror symmetry are highlighted and indicate the violation of cubic symmetry of the structure.

Table S1. Crystal data and structure refinement for Co₃S₂Sn₂ at room temperature.

Empirical formula	Co ₃ S ₂ Sn ₂
Temperature	295(2) K
Wavelength	0.71073 Å
Crystal system	Trigonal
Space group	<i>R</i> -3 <i>m</i> : H
Unit cell dimensions	<i>a</i> = 5.3689(5) Å <i>c</i> = 13.176(2) Å (<i>a</i> = 5.3757(6) Å, α = 59.916(8)° for primitive cell)
Volume	328.92(8) Å ³
<i>Z</i>	3
Density (calculated)	7.244 g/cm ³
Absorption coefficient	23.089 mm ⁻¹
F(000)	639
Crystal size	0.074 × 0.076 × 0.135 mm ³
Theta range for data collection	4.65 to 34.7°
Index ranges	-4 ≤ <i>h</i> ≤ 8, -7 ≤ <i>k</i> ≤ 8, -17 ≤ <i>l</i> ≤ 21
Reflections collected	868
Independent reflections	195 [<i>R</i> (int) = 0.0223]
Refinement method	Full-matrix least-squares on F ²
Data / restraints / parameters	195 / 0 / 13
Goodness-of-fit on F ²	1.282
Final <i>R</i> indices [<i>I</i> > 2σ(<i>I</i>)]	<i>R</i> 1 = 0.0224, <i>wR</i> 2 = 0.0546
<i>R</i> indices (all data)	<i>R</i> 1 = 0.0226, <i>wR</i> 2 = 0.0547
Extinction coefficient	0.061(3)

2.2 Topographic images from scanning tunneling microscopy

The high quality of the single crystals was further confirmed by scanning tunneling microscopy (STM) showing topographic image of the hexagonal array of the (0001) crystal surface.

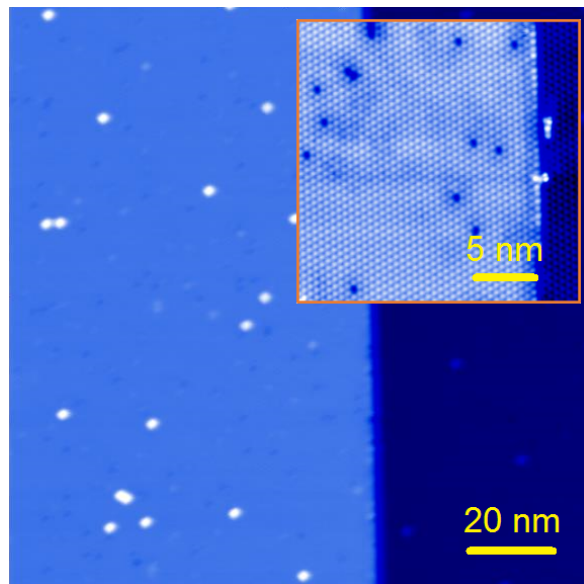


Fig. S3. STM real-space topographic image of the (0001) surface, obtained after *in situ* low-temperature cleaving. The inset is a $20 \times 20 \text{ nm}^2$ topography showing a hexagonal array, which shows nice atomic resolution. A sharp step edge with a height of $\sim 80 \text{ pm}$ is resolved.

3. Magnetic measurements

3.1 Basic magnetic behaviours

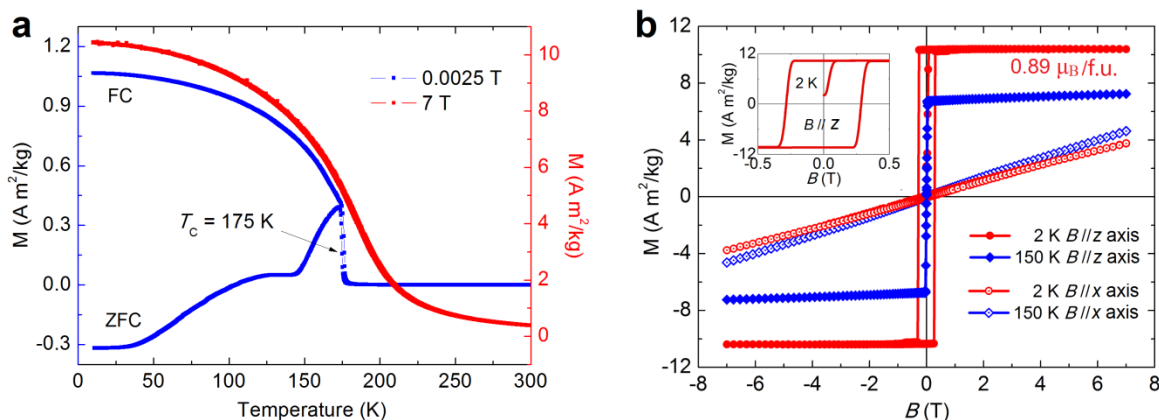


Fig. S4. Magnetic measurements. (a) ZFC/FC measurements on temperature dependence of magnetization. The Curie temperature is located at $T_c = 175$ K. Around 140 K, there is an anomalous magnetic transition around 150 K at low field of 0.0025 T (25 Oe) in the ZFC curve. However, this transition has been suppressed during the FC measurement. In higher fields, this weak transition also disappears, which deserves further study. (b) Field dependence of magnetization at 2 and 150 K with field along x (a) and z (c) axes. Inset shows the magnetization loop with a hysteresis at 2 K with field along z axis. The field dependence of magnetization indicates there is a strong magneto-crystalline anisotropy in this compound with the moment along c -axis. Along c -axis, the magnetization rapidly saturates at a low field of 0.1 T. In a - b plane, the magnetization does not show any sign of saturation in magnetic fields up to 7 T. At 2 K, a saturated moment of $0.89 \mu_B/\text{f.u.}$ ($0.30 \mu_B/\text{Co}$) was observed in easy axis.

3.2 On the strong magnetic anisotropy

According to the magnetization measurements, one can see this material shows an extremely strong magnetic anisotropy. We would like to present our understanding on this behaviour.

In $\text{Co}_3\text{Sn}_2\text{S}_2$, there are two different types of valence for Co atom. One is Co^{0+} for metallic Co-Sn bonding, and the other is Co^{2+} for covalent/ionic Co-S bondings⁴. For Co-S bonding, it is reported that there are strong correlations between electrons. LSDA + U calculations furthermore suggest a layered structural nature of the electron density distribution.

Actually, another experimental study⁵ showed that replacing S by large-size Se results in a decrease of T_c and coercive force of $\text{Co}_3\text{Sn}_2\text{S}_2$, which gives a significant hint that the spins are inverted more easily as a direct effect of weakened coupling between the Co layers. At the same time, the so-called electron correlations in Co-S bonding become weaker upon changing to Co-

Se bonding. This indicates a strong anisotropy in magnetic exchange interactions for this material.

Besides, a recent study⁶ revealed that the ratio of effective and saturation magnetizations (p_{eff}/p_s) and the scaled Curie temperature (t_c) of the $\text{Co}_3\text{Sn}_2\text{S}_2$ Shandite is much smaller than that expected from the universal relation for weak itinerant-electron ferromagnets (WIEFs). More specifically, it indicates that the ferromagnetism in the Co-based Shandite $\text{Co}_3\text{Sn}_2\text{S}_2$ is much weaker than in conventional 3D WIEFs. We speculate that this is manifestation of the quasi-2D character of $\text{Co}_3\text{Sn}_2\text{S}_2$ owing to its layered crystal structures.

Taken together, the layered crystal structure of $\text{Co}_3\text{Sn}_2\text{S}_2$ results in strongly anisotropic electronic states and consequently quasi-2D character in the electronic and magnetic properties. In particular, this also results in a strong magnetic anisotropy.

4. Topological electronic structures by theoretical calculations

The electronic calculations were carried out based on the density functional theory using the Vienna *ab-initio* simulation package (VASP)⁷. The exchange and correlation energies were treated under the gradient approximation (GGA), following the Perdew–Burke–Ernzerhof parametrization scheme⁸. The calculations were performed using the experimentally measured lattice parameters in this study ($a = 5.3689 \text{ \AA}$ and $c = 13.176 \text{ \AA}$).

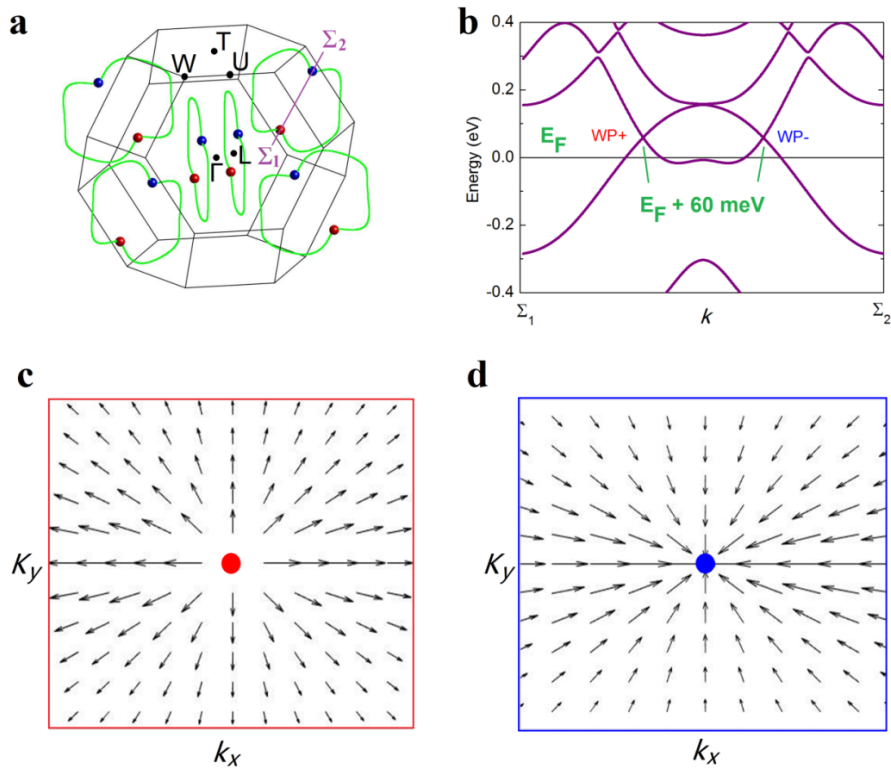


Fig. S5. Topological electronic structures. (a) Distribution of nodal lines in the BZ. A cut from Σ_1 to Σ_2 is shown. (b) band structure along Σ_1 - Σ_2 path. Under SOC, a pair of linear crossings of Weyl points (WP+ and WP-) is presented at 60 meV above the Fermi level. The positions of WP+ and WP- of the momenta (k_x, k_y, k_z) are $2\pi (0.461/a, 0, 0.140/c)$ and $2\pi (0.693/a, 0, 0.960/c)$, respectively. **c** and **d**, sink and source of the monopoles of the Berry curvature at WP+ and WP- points, respectively. The topological charge is +1 and -1, respectively.

5. Dominating Berry curvature contribution to the intrinsic AHE

Since the intrinsic AHC is determined by the integral of the Berry curvature in the whole Brillouin zone, the best way to see the dominating contribution to AHE is to consider the Berry curvature distribution in k -space. Our calculations show that large Berry curvature arises mainly from the nodal-line like band anti-crossing (see Fig. 2 (d-e) in the main manuscript). Though the Berry curvature is not zero in some areas away from the nodal lines, it is rather very small compared to that from the nodal lines.

Furthermore, since the symmetry requirement for the existence of Weyl points is just the lattice translation symmetry, the only way to remove the Weyl points is to move one pair of Weyl points with opposite chirality to meet each other⁹. In the case of $\text{Co}_3\text{Sn}_2\text{S}_2$, owing to the mirror symmetry and ferromagnetic structure, there are two important results for the band inversion: nodal lines and Weyl points. The only way to kill the Weyl points is to move this one pair of Weyl points on the nodal rings to the same k -point (see Fig. 2(b) in the main manuscript), which also removes the band inversion and nodal rings.

We further show the Berry curvature contribution to the intrinsic AHE, as shown in Fig. S6. The Berry curvature contribution is dominated by the nodal lines. Though there are some contributions from other areas, such as L and T points, they are very weak in comparison to those from the nodal lines. Therefore, the large Berry curvature from the nodal rings and Weyl points is robust as long as the band inversion is present.

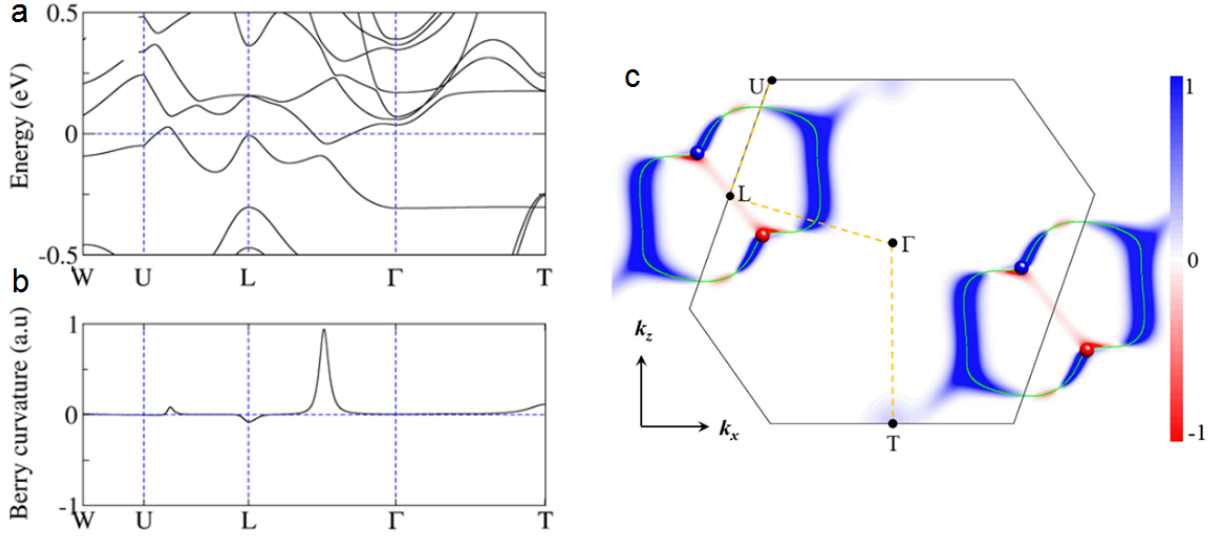


Fig. S6. Berry curvature contribution to AHE. (a) Electronic band structure (b) Berry curvature ($\Omega_{yx}^z(\vec{k})$) of $\text{Co}_3\text{Sn}_2\text{S}_2$ along high symmetry paths. (c) Berry curvature distribution in $k_y=0$ plane.

6. ARPES results and comparison with theoretical calculations

In order to check the accuracy of the DFT calculations, we also performed the angle resolved photoemission spectroscopy (ARPES) measurements on $\text{Co}_3\text{Sn}_2\text{S}_2$. We show a comparison of the k_z projected Fermi surface and energy dispersion along high symmetry lines of $\bar{M} - \bar{\Gamma} - \bar{M}$ and $\bar{K} - \bar{\Gamma} - \bar{K}$ between calculations and ARPES measurements. Fixing the energy at the Fermi level, one can see the good agreement of the Fermi surfaces from ARPES measurements and DFT calculations, as indicated in Fig. S7(b). Besides, the good agreement is also obtained for the energy dispersion along high symmetry lines in a large energy window, see Fig. S7(c-d).

Though the Weyl nodes above the Fermi level cannot be observed from the present ARPES results, the DFT calculation is accurate enough to explain the Weyl-related non-trivial intrinsic property of $\text{Co}_3\text{Sn}_2\text{S}_2$.

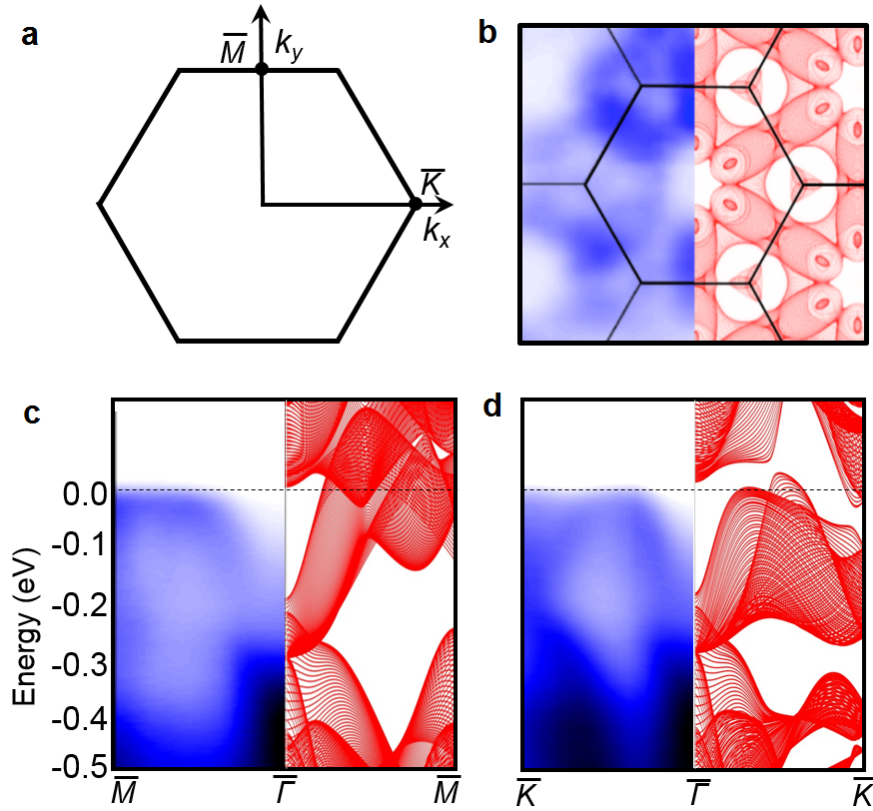


Fig. S7. Comparison of band structure between ARPES measurements and DFT calculations on $\text{Co}_3\text{Sn}_2\text{S}_2$. (a) Projected 2D Brillouin zone along z direction. (b) Comparison of Fermi surface (FS) between ARPES measurements (left) and DFT (right) calculations. (c, d) Comparisons of the energy dispersions between ARPES measurements (left) and DFT calculations (right) along $\bar{M} - \bar{\Gamma} - \bar{M}$ and $\bar{K} - \bar{\Gamma} - \bar{K}$, respectively. The calculated bulk energy dispersions are projected to k_z .

7. Transport measurements

In this study, the out-of-plane and angle-dependent transport measurements were performed, and the currents were always applied along the a -axis, e.g. $I // x // [2\bar{1}\bar{1}0]$ (a axis = x axis), as shown in Fig. S8. For the out-of-plane configuration, $B // z // [0001]$ and $I // x // [2\bar{1}\bar{1}0]$. For the angle-dependent case, $B // \theta$ and $I // x // [2\bar{1}\bar{1}0]$, θ is the angle with respect to $x // [2\bar{1}\bar{1}0]$. Different crystals, grown by two self-flux methods and with different RRR ($\rho_{300\text{K}}/\rho_{2\text{K}}$) values, were used in this study.

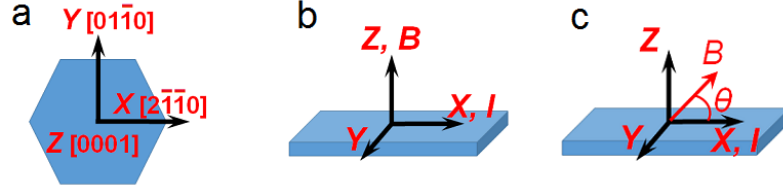


Fig. S8. Sample schematic for transport measurements. (a) schematic for crystals and orientations. (b) Out-of-plane configuration. $B \parallel z \parallel [0001]$ and $I \parallel x \parallel [2\bar{1}\bar{1}0]$. The longitudinal charge resistivity and Hall resistivity were measured along x and y axes, respectively. (c) Angle-dependent transport configuration. θ is the angle with respect to $x \parallel [2\bar{1}\bar{1}0]$. The Hall resistivity were measured along y axis.

We used the five-probe method to measure the Hall signal to try to balance the longitudinal voltage drops. However, in practical measurements there still is weak longitudinal voltage drops. In order to obtain the accurate Hall data, we further applied the procedure of (anti-) symmetrization to extract the odd and even parts of the observed signal. For longitudinal charge resistivity, the ρ - B is odd and ρ_{H-B} is even, and we can extract the pure Hall component using $\rho_H = [\rho_H(B) - \rho_H(-B)]/2$, while the pure charge resistivity component using $\rho = [\rho(B) + \rho(-B)]/2$. The extracted results are shown in Fig. S9. The saturation and coercive fields of the loop behaviour for magnetization and Hall resistivity were determined by magnetic and transport measurements, as shown in Fig. S10.

There is a transition of carrier type in $\text{Co}_3\text{Sn}_2\text{S}_2$ with temperature. At high temperatures ($50 \text{ K} < T < T_C$), the Hall signal shows a linear field-dependent behaviour after saturation (see Fig. S11a). Hole carriers dominate the transport. At low temperatures ($T < 50 \text{ K}$), a notable non-linear field dependence of the Hall resistivity is observed (see Fig. 1f in the main manuscript). This indicates the coexistence of hole and electron carriers. The electron carriers appear at low temperatures. The single-band and two-band models were thus applied to extract the pure anomalous Hall resistivity, carrier densities and mobilities, for high-temperature and low-temperature cases, respectively.

The pure anomalous Hall resistivity (ρ_H^A) was derived by extrapolating the high-field part of ρ_H back to zero field for the data recorded above 50 K, as shown in Fig. S11. The anomalous Hall conductivity was calculated by $\sigma_H^A = -\rho_H^A/((\rho_H^A)^2 + \rho^2)$. Here ρ_H^A is the anomalous Hall resistivity at zero field; ρ is the longitudinal charge resistivity at zero field. The σ dependence of σ_H^A of our material has been discussed in the framework of unified model, as shown in Fig. S12.

The semi-metallicity of $\text{Co}_3\text{Sn}_2\text{S}_2$ is investigated. First, a resistance increase in the high magnetic fields is observed at low temperatures (Fig. 1d in the main manuscript). This exhibits the common behavior of semi-metallic materials. The positive, non-saturated magnetoresistance (MR) observed (Fig. 1e in the main manuscript) indicates a semi-metallic behaviour^{10,11}. From

the Hall data measured at 2 K (Fig. 1f in the main manuscript), we further observe a notable non-linear behaviour of the Hall trace with increasing magnetic field, indicating the existence of two types of carriers (electrons and holes). Indeed, the theoretical calculations (Fig. 1b in the main manuscript) indicate there are two relatively small Fermi surfaces of holes and electrons.

We thus applied the two-band model¹² below to extract the densities of both carriers.

$$\sigma(B) = \frac{n_h e \mu_h}{1 + \mu_h^2 B^2} + \frac{n_e e \mu_e}{1 + \mu_e^2 B^2}$$

$$\sigma_H(B) = \frac{n_h e \mu_h^2 B}{1 + \mu_h^2 B^2} + \frac{n_e e \mu_e^2 B}{1 + \mu_e^2 B^2}$$

Here B is applied magnetic field, $\sigma(B)$ is longitudinal charge conductivity, $\sigma_H(B)$ is anomalous Hall effect, n_h is carrier concentration of holes and μ_h is carrier mobility of holes, n_e is carrier concentration of electrons and μ_e is carrier mobility of electrons.

The best-fitted results are as follows:

$$n_h = 9.3 \times 10^{19} \text{ cm}^{-3}, \mu_h = 6.4 \times 10^2 \text{ cm}^2 \text{ V}^{-1} \text{ s}^{-1},$$

$$n_e = 7.6 \times 10^{19} \text{ cm}^{-3}, \mu_e = 7.3 \times 10^2 \text{ cm}^2 \text{ V}^{-1} \text{ s}^{-1}.$$

The densities of holes and electrons thus obtained - as well as the total charge carrier density - are not high. Furthermore, the holes and electron densities are closely comparable in magnitude. These relatively low carrier densities further confirm the semi-metallicity of $\text{Co}_3\text{Sn}_2\text{S}_2$ with near compensated carriers. The related results at 2 K are shown in Table S2.

Table S2. Longitudinal charge resistivity (ρ), longitudinal charge conductivity (σ), anomalous Hall effect (ρ^{A_H}), carrier concentration (n_h) and carrier mobility (μ_h) of holes, carrier concentration (n_e) and carrier mobility (μ_e) of electrons in a sample, recorded at 2 K.

ρ (ρ_{xx})	σ (σ_{xx})	ρ^{A_H}	n_h	μ_h	n_e	μ_e
$\mu\Omega \text{ cm}$	$10^4 \Omega^{-1} \text{ cm}^{-1}$	$\mu\Omega \text{ cm}$	10^{19} cm^{-3}	$10^2 \text{ cm}^2 \text{ V}^{-1} \text{ s}^{-1}$	10^{19} cm^{-3}	$10^2 \text{ cm}^2 \text{ V}^{-1} \text{ s}^{-1}$
49.96	2.00	2.80	9.3	6.4	7.5	729

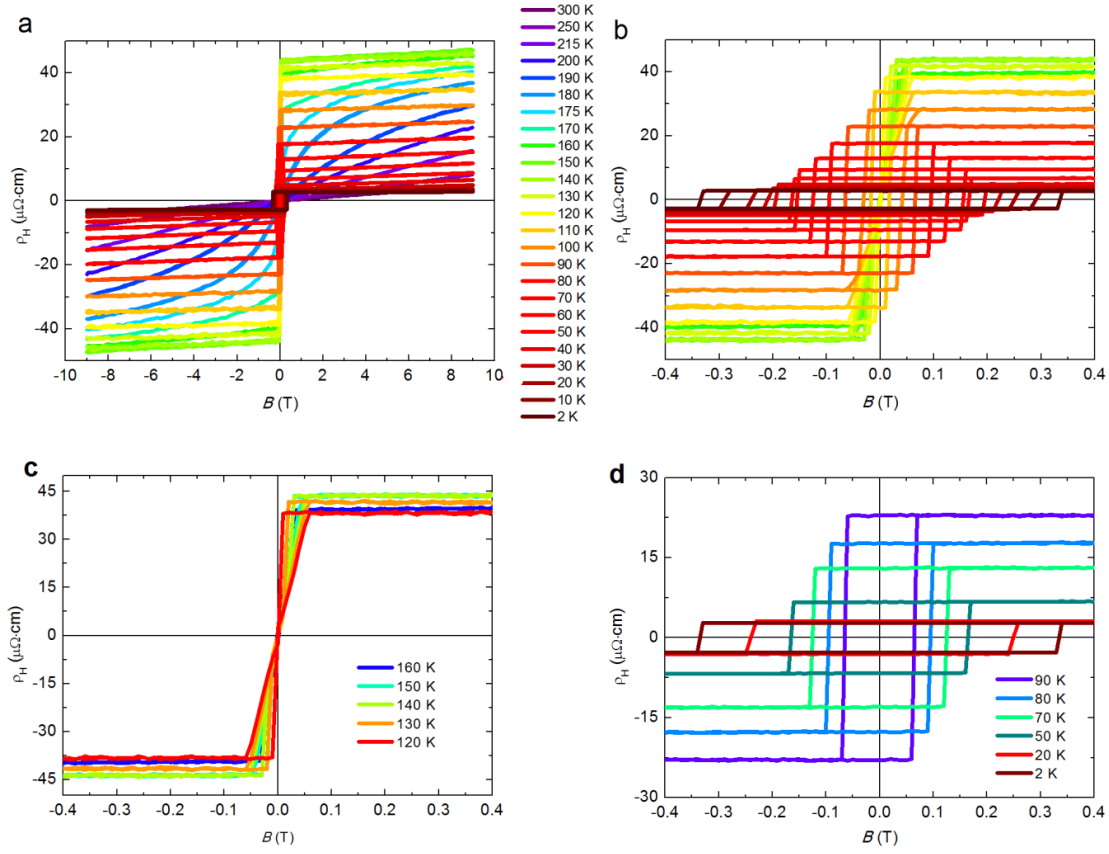


Fig. S9. Field dependence of Hall resistivity (ρ_H). (a) All data measured in $-9 \sim 9$ T from 300 to 2 K. (b) Data measured in $-0.4 \sim 0.4$ T from 300 to 2 K. (c) Data measured in $-0.4 \sim 0.4$ T from 160 to 120 K. (d) Data measured in $-0.4 \sim 0.4$ T from 100 to 2 K. A maximum of Hall resistivity appears around 150 K. A hysteresis appears below 150 K and a coercive field can be observed below 120 K. The coercive field increases with decreasing temperature, as shown in Fig. S10. Below 100 K, a sharp switch with a rectangle shape in Hall resistivity loop can be seen owing to the switching of magnetization and Berry curvature.

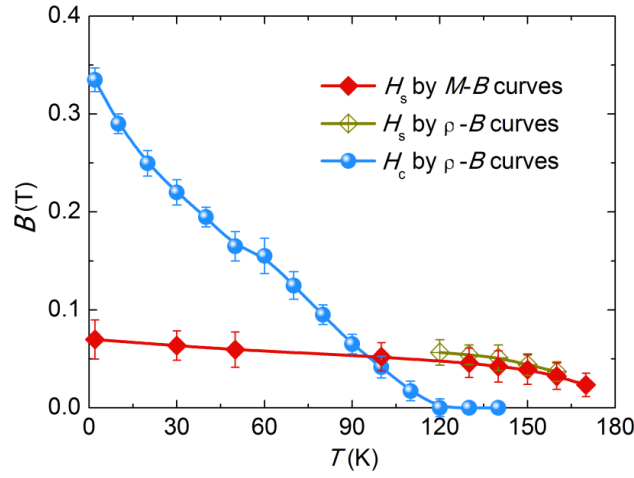


Fig. S10. Saturation and coercive fields. The loop behaviours of magnetization and Hall resistivity were determined by magnetic and transport measurements.

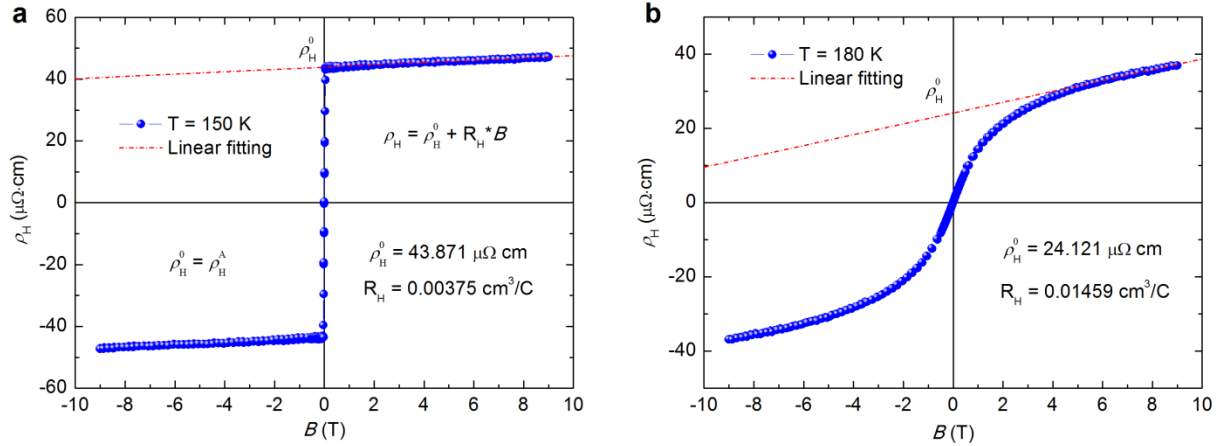


Fig. S11. Deriving the pure anomalous Hall resistivity ($\rho_H^A = \rho_H^0$) by extrapolating the high-field part of ρ_H back to zero field for the data recorded above 50 K. (a) $T = 150$ K, below T_C . (b) $T = 180$ K, slightly above T_C . The ordinary Hall contribution vanishes at zero field, only the anomalous contribution prevails. Only demonstrations at two temperatures were shown here.

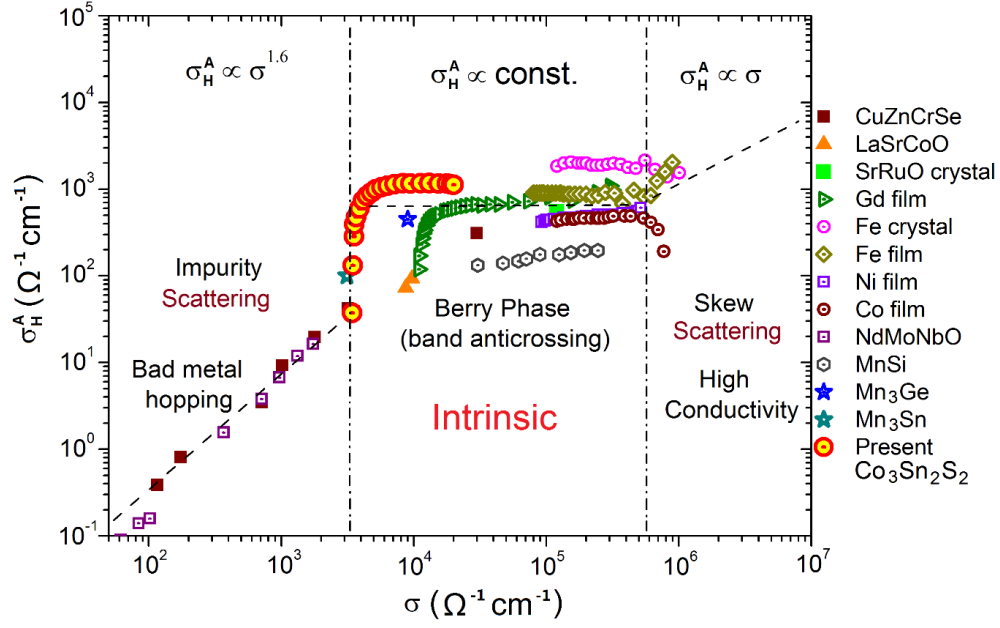


Fig. S12. σ dependence of σ_H^A in the framework of unified model^{13,14}. Here we use the absolute amplitudes of σ_H^A without the negative sign. The data of other materials were taken from references and therein^{15,16}. Our present result shows a σ -independent σ_H^A below 100 K, i.e., $\sigma_H^A \sim (\sigma)^0 = \text{constant}$. Our data matches the prediction of the model. $\text{Co}_3\text{Sn}_2\text{S}_2$ is located into the intrinsic regime dominated by the Berry-phase curvature, not by the extrinsic scattering events. Here the Berry-phase curvature just comes from the Weyl nodes and gapped nodal lines with band anticrossing in $\text{Co}_3\text{Sn}_2\text{S}_2$.

8. Anomalous Hall conductivity-dependence of anomalous Hall angle (AHA)

Comparison of our σ_H^A -dependent AHA results and previously reported data for other AHE materials was performed. The reported data were taken from references that can be found in Table S3.

Table S3. Summary of longitudinal charge conductivity (σ), anomalous Hall conductivity (σ_H^A), and anomalous Hall angle (AHA) of currently studied magnetic materials. Some AHA values are calculated by using the data from the references. Here we use the absolute amplitudes of σ_H^A without the negative sign. Only the maximum values of AHA are adopted here.

System	σ	σ_H^A	AHA= σ_H^A/σ	Refs.
	$10^4 \Omega^{-1} \text{ cm}^{-1}$	$\Omega^{-1} \text{ cm}^{-1}$	%	
Mn ₃ Ge	0.90	450	5.0	17
Mn ₃ Sn	0.31	100	3.2	18
GdPtBi	0.07	110	16	19
Fe ₃ Sn ₂	10.0	1100	1.1	20
MnGa film	0.51	288	5.7	21
L1 ₀ -FePt film	3.79	1250	3.3	22
TbCo film	2.50	800	3.2	23
Mn ₂ Ru _x Ga	0.29	220	7.7	24
SmFe film	0.66	317	4.8	25
Fe _{0.28} TaS ₂	0.90	336	3.7	26
GaMnAs film	0.22	147	6.6	27
SrRuO ₃ film	2.00	200	1.0	28
Co ₂ FeSi	1.18	208	1.8	29
Co ₂ FeAl	0.96	120	1.3	29
Fe film	4.36	1134	2.6	14
Gd film	50.00	1000	0.2	14
LaSrCoO	1.00	100	1.0	14
CuZnCrSe	5.00	500	1.0	14
MnSi	0.40	150	3.8	30
Mn ₅ Ge ₃	1.41	860	6.1	31
Co₃Sn₂S₂	0.57	1130	19.8	Present work

9. Shubnikov-de Haas (SdH) quantum oscillations

The magnetoresistance was measured with current along a -axis and magnetic field along c -axis in static high magnetic fields up to 37 T at low temperatures. The SdH oscillations have been observed in Fig. S13a. The oscillations are clearly visible by subtracting a cubic polynomial from the resistivity data. The extracted amplitudes of the SdH oscillations as a function of the inverse magnetic field are shown in Fig. S13b. The fast Fourier transform (FFT) of the SdH oscillations identifies two fundamental frequencies at 104 T (α) and 198 T (β). It can be seen that the amplitude of the peak corresponding to 198 T decreases rapidly with temperature compared to the 104 T peak. We fit the temperature dependent peak amplitudes with the Lifshitz-Kosevich formula to obtain effective mass of $0.98m_0$ and $3.9m_0$ for 104 T and 198 T frequencies, respectively.

The extremal cross section area of the Fermi surface perpendicular to the applied magnetic field is directly related to the frequency of the quantum oscillations. We further performed the calculations on the energy dependence of frequency with magnetic field along c -axis. Figure S14 shows some related frequencies. In Fig S14b and c, we can see hole (H3) and electron (E1) pockets show the frequency around 200 T. Considering the possible self p-doping of the real material, the Fermi level will decrease. In this case, if the Fermi level decreases by 0.025 eV, there are just two calculated frequencies corresponding to our measurements, as shown in Fig. S14c and d. One is ~ 198 T and the other is ~ 104 T, which are consistent with the observed frequencies in measurements.

As expected in semimetals, $\text{Co}_3\text{Sn}_2\text{S}_2$ shows the SdH oscillations in high magnetic fields. The measured and calculated frequencies are consistent with each other, considering the possible p-doping. The corresponding effective masses are $0.98m_0$ and $3.9m_0$, respectively. Having known the frequency and effective mass of two fermi pockets we can determine various parameters crucial for the electrical transport considering the Fermi surface is not very anisotropic. Using the Onsager relation one can find the extremal area, $A_F = \left(\frac{2\pi e}{\hbar}\right)F$. The Fermi wave vector k_F can be calculated by the relation $A_F = \pi(k_F)^2$. Using the value of effective mass, k_F we calculate the Fermi velocity as $v_F = \hbar k_F / m^*$. The Fermi energy is then calculated as $E_F = \frac{1}{2} m^* v_F^2$. We tabulate all these quantities for the two fermi surfaces in Table S4.

Table S4. Extremal area (A_F), Fermi wave vector (k_F), Fermi velocity (v_F), Fermi energy (E_F) related to Fermi surface. α and β are two Fermi surfaces. F is the oscillation frequency.

Fermi surface	F (T)	m^* (m_0)	A_F (\AA^{-2})	K_F (\AA^{-1})	v_F (m/s)	E_F (meV)
α	104	0.98	0.01	0.056	6.6×10^4	12.3
β	198	3.9	0.019	0.078	2.3×10^4	5.9

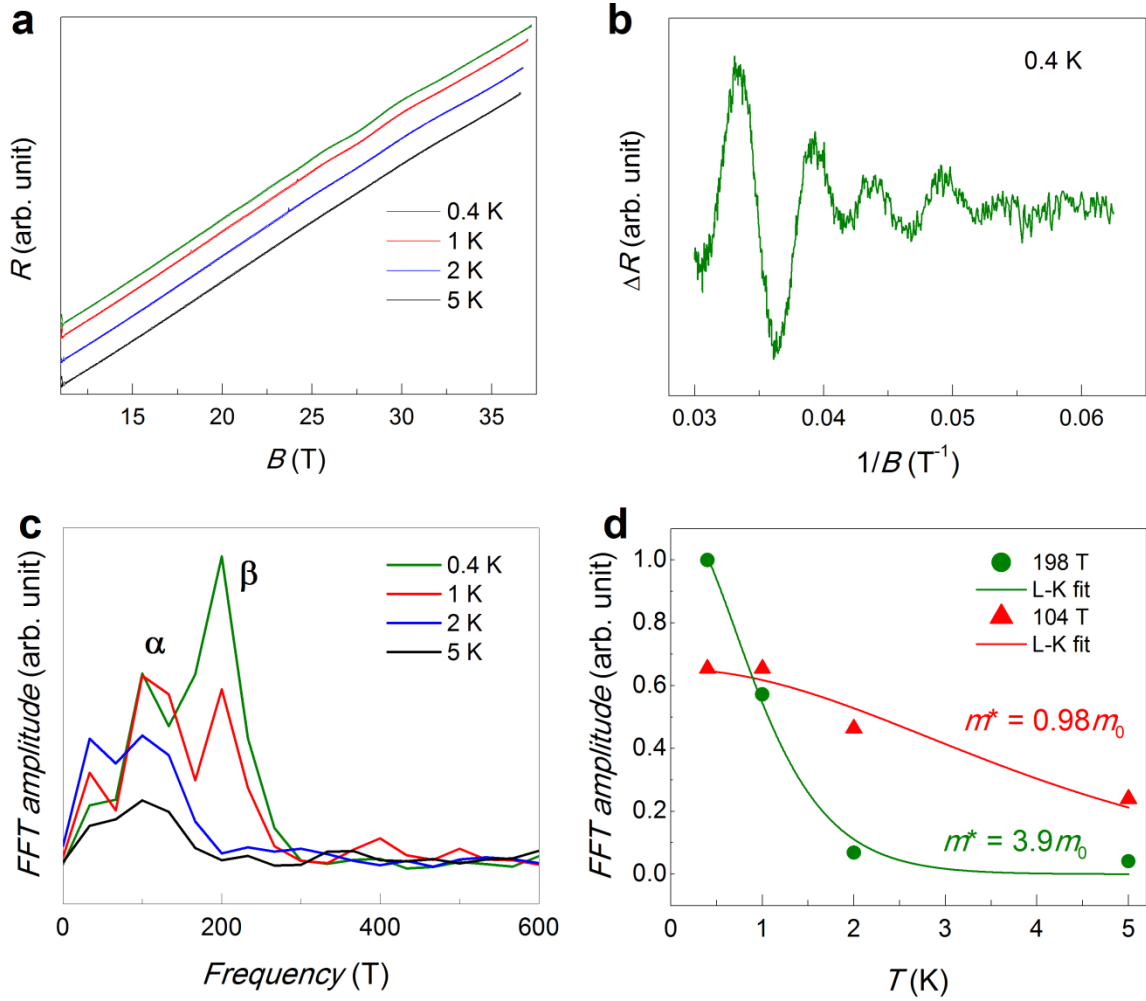


Fig. S13. SdH oscillations in $\text{Co}_3\text{Sn}_2\text{S}_2$. (a) MR data at different temperatures from 0.4 - 5 K with quantum oscillations. (b) Corresponding SdH oscillations amplitudes obtained by subtracting a cubic polynomial. (c) FFT amplitudes as a function of the temperature showing two fundamental frequencies at 104 T and 198 T. (d) Effective mass evaluation by fitting temperature-dependent FFT amplitudes by Lifshitz-Kosevich formula.

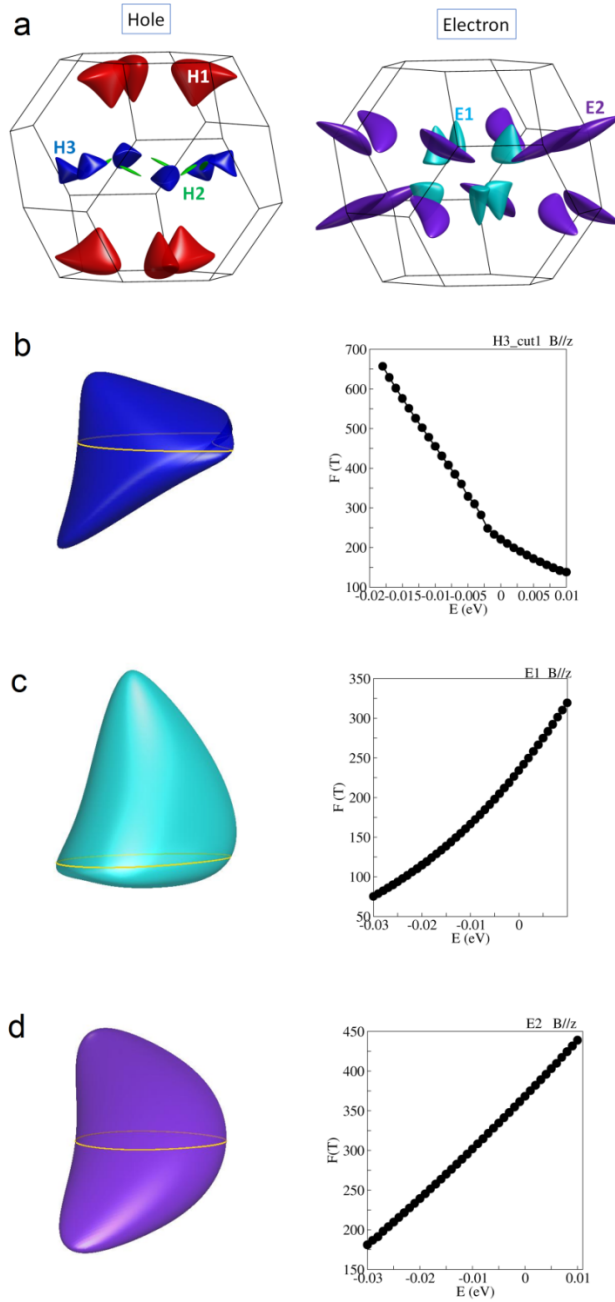


Fig. S14. Calculated Fermi surfaces and the frequencies of the quantum oscillations of carriers on Fermi surfaces. (a) The calculated Fermi surfaces of holes and electrons. Hole pocket H3 (b), electron pocket E1 (c), electron pocket E2 (d) and corresponding calculated energy dependences of frequency with magnetic field along z -axis.

10. Non-collinear magnetic structures

Inspired by the weak anomalous magnetic transition (Fig. S4a) in this Kagomé-lattice compound, we further considered the possible non-collinear magnetic structures. We increased the angle with respect to c -axis and changed the collinear structure to non-collinear ones. With increasing tilting angle, we found the total energy increases. Figure S15 shows a comparison between collinear (along c -axis) and special non-collinear (along Co-S bonding) magnetic structures. The total energy difference between two cases is small. Both cases have anomalous Hall conductivity $\sigma_{yx} > 1000 \Omega^{-1} \text{cm}^{-1}$ and the σ_{yx} are close to each other. These results mean the existence of Weyl points and large σ_{yx} are robust against the change of magnetic structure in $\text{Co}_3\text{Sn}_2\text{S}_2$.

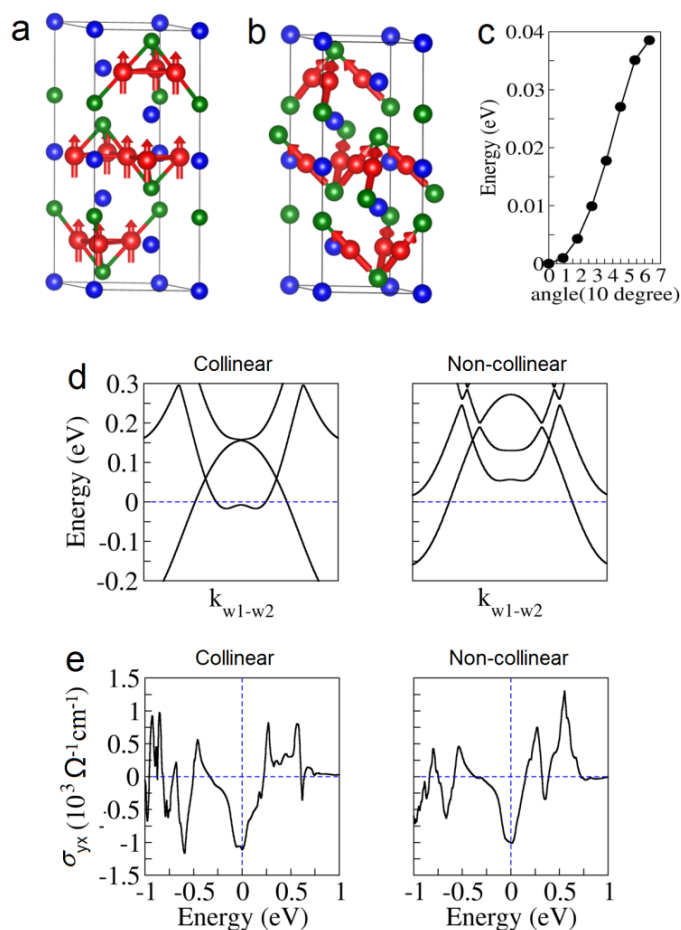


Fig. S15. Comparison of linear and non-collinear magnetic structures. (a) Collinear magnetic structure with atom moments along c -axis. (b) An example of non-collinear magnetic structure, with atom moments along the Co-S bonding. (c) Total energy evolution as a function of titled angle of atom moments with respect to c -axis. (d) Energy dispersion along one pair of Weyl nodes with collinear magnetic and non-collinear magnetic structures as given in (a, b). (e) Energy dependent σ_{yx} for collinear and non-collinear magnetic structures as given in (a, b).

Supplementary References

1. Lin, X., Bud'ko, S. L. and Canfield, P. C. Development of viable solutions for the synthesis of sulfur bearing single crystals. *Philos. Mag.* **92**, 2436-2447 (2012).
2. Schnelle, W. *et al.* Ferromagnetic ordering and half-metallic state of $\text{Sn}_2\text{Co}_3\text{S}_2$ with the Shandite-type structure. *Phys. Rev. B* **88**, 144404 (2013).
3. Kassem, M. A., Tabata, Y., Waki, T. and Nakamura, H. Single crystal growth and characterization of kagomé-lattice shandites $\text{Co}_3\text{Sn}_{2-x}\text{In}_x\text{S}_2$. *J. Crystal Growth* **426**, 208-213 (2015).
4. Umetani, A., Nagoshi, E., Kubodera, T. and Matoba, M. Electronic and magnetic nature of shandite-type $\text{A}_2\text{Co}_3\text{S}_2$ (A=Sn,In). *Physica B: Condensed Matter* **403**, 1356-1358 (2008).
5. Weihrich, R. *et al.* Tuneable anisotropy and magnetism in $\text{Sn}_2\text{Co}_3\text{S}_{2-x}\text{Se}_x$ - probed by ^{119}Sn Mößbauer spectroscopy and DFT studies. *Dalton Trans.* **44**, 15855-15864 (2015).
6. Kassem, M. A., Tabata, Y., Waki, T. and Nakamura, H. Quasi-two-dimensional magnetism in Co-based Shandites. *J. Phys. Soc. Jpn.* **85**, 064706 (2016).
7. Kresse, G. and Furthmüller, J. Efficient iterative schemes for *ab initio* total-energy calculations using a plane-wave basis set. *Phys. Rev. B* **54**, 11169-11186 (1996).
8. Perdew, J. P., Burke, K. and Ernzerhof, M. Generalized gradient approximation made simple. *Phys. Rev. Lett.* **77**, 3865-3868 (1996).
9. J. von Neuman and Wigner, E. Über merkwürdige diskrete Eigenwerte. Über das Verhalten von Eigenwerten bei adiabatischen Prozessen. *Phys. Z.* **30**, 467 (1929).
10. Ali, M. N. *et al.* Large, non-saturating magnetoresistance in WTe_2 . *Nature* **514**, 205-208 (2014).
11. Kumar, N. *et al.* Extremely high magnetoresistance and conductivity in the type-II Weyl semimetals WP_2 and MoP_2 . *Nat. Commun.* **8**, 1642 (2017).
12. Ziman, J. M., *Electrons and Phonons: Theory of Transport Phenomena in Solids.* (Oxford University Press, 1960).
13. Onoda, S., Sugimoto, N. and Nagaosa, N. Intrinsic versus extrinsic anomalous Hall effect in ferromagnets. *Phys. Rev. Lett.* **97**, 126602 (2006).
14. Miyasato, T. *et al.* Crossover behavior of the anomalous Hall effect and anomalous Nernst effect in itinerant ferromagnets. *Phys. Rev. Lett.* **99**, 086602 (2007).
15. Onoda, S., Sugimoto, N. and Nagaosa, N. Quantum transport theory of anomalous electric, thermoelectric, and thermal Hall effects in ferromagnets. *Phys. Rev. B* **77**, 165103 (2008).
16. Asamitsu, A. *et al.* Anomalous Hall effect and Nernst effect in itinerant ferromagnets. *J. Magn. Magn. Mater.* **310**, 2000-2002 (2007).
17. Nayak, A. K. *et al.* Large anomalous Hall effect driven by a nonvanishing Berry curvature in the noncolinear antiferromagnet Mn_3Ge . *Sci. Adv.* **2**, e1501870 (2016).
18. Nakatsuji, S., Kiyohara, N. and Higo, T. Large anomalous Hall effect in a non-collinear antiferromagnet at room temperature. *Nature* **527**, 212 (2015).

19. Suzuki, T. *et al.* Large anomalous Hall effect in a half-Heusler antiferromagnet. *Nat. Phys.* **12**, 1119-1123 (2016).
20. Ye, L. *et al.* Massive Dirac fermions in a ferromagnetic kagome metal. *Nature* **555**, 638 (2018).
21. Wu, F. *et al.* Electrical transport properties of perpendicular magnetized Mn-Ga epitaxial films. *Appl. Phys. Lett.* **96**, 042505 (2010).
22. Yu, J. *et al.* Magnetotransport and magnetic properties of molecular-beam epitaxy L1₀ FePt thin films. *J. Appl. Phys.* **87**, 6854-6856 (2000).
23. Kim, T. W. and Gambino, R. J. Composition dependence of the Hall effect in amorphous Tb_xCo_{1-x} thin films. *J. Appl. Phys.* **87**, 1869-1873 (2000).
24. Thiagarajah, N. *et al.* Giant spontaneous Hall effect in zero-moment Mn₂Ru_xGa. *Appl. Phys. Lett.* **106**, 122402 (2015).
25. Kim, T. W., Lim, S. H. and Gambino, R. J. Spontaneous Hall effect in amorphous Tb-Fe and Sm-Fe thin films. *J. Appl. Phys.* **89**, 7212-7214 (2001).
26. Dijkstra, J., Zijlema, P. J., Bruggen, C. F. v., Haas, C. and Groot, R. A. d. Band-structure calculations of Fe_{1/3}TaS₂ and Mn_{1/3}TaS₂, and transport and magnetic properties of Fe_{0.28}TaS₂. *J. Phys.: Condens. Matter* **1**, 6363 (1989).
27. Pu, Y., Chiba, D., Matsukura, F., Ohno, H. and Shi, J. Mott relation for anomalous Hall and Nernst effects in Ga_{1-x}Mn_xAs ferromagnetic semiconductors. *Phys. Rev. Lett.* **101**, 117208 (2008).
28. Fang, Z. *et al.* The anomalous Hall effect and magnetic monopoles in momentum space. *Science* **302**, 92-95 (2003).
29. Imort, I. M., Thomas, P., Reiss, G. and Thomas, A. Anomalous Hall effect in the Co-based Heusler compounds Co₂FeSi and Co₂FeAl. *J. Appl. Phys.* **111**, 07D313 (2012).
30. Manyala, N. *et al.* Large anomalous Hall effect in a silicon-based magnetic semiconductor. *Nat. Mater.* **3**, 255 (2004).
31. Zeng, C., Yao, Y., Niu, Q. and Weitering, H. H. Linear magnetization dependence of the intrinsic anomalous Hall effect. *Phys. Rev. Lett.* **96**, 037204 (2006).